processes

MDPI

Article

Investigation on Energy-Effectiveness Enhancement of Medium-Frequency Induction Furnace Based on an Adaptive Chaos Immune Optimization Algorithm with Mutative Scale

Hongyan Zuo [1], Yun Zhu [1], Dongli Tan [2,*], Shuwan Cui [2], Jiqiu Tan [1] and Dingqing Zhong [1]

[1] School of Mechanical Engineering, Hunan Institute of Engineering, Xiangtan 411104, China; zuohongyan@hnie.edu.cn (H.Z.); zhuyun_hnu@163.com (Y.Z.); tan058@sina.com (J.T.); zhdiqi@126.com (D.Z.)
[2] School of Mechanical and Automotive Engineering, Guangxi University of Science and Technology, Liuzhou 545006, China; swcui@gxust.edu.cn
* Correspondence: tandongli@gxust.edu.cn

Abstract: Based on the chaos algorithm and immune algorithm theory, an adaptive chaotic immune optimization algorithm (ACIOA) with a mutative scale was proposed and subsequently validated by the experiment result in this paper, and then the adaptive chaotic immune optimization algorithm with mutative scale was applied to investigate the performance characteristics of the medium-frequency induction furnace. The obtained results include the effects on the performance characteristics of a medium-frequency induction furnace of the diameter of the heated cylindrical material, the thickness of the crucible wall, the fullness degree of the induction coil, the ratio of diameter to current penetration depth, and the power frequency. The results showed that the optimization algorithm could continuously modify the variable search space and take the optimal number of cycles as the control index to carry out the search. In addition, the suitable ratio of diameter to current penetration depth was between 3.5 and 6.0, and was beneficial to the improvements of in power factor and thermal efficiency. This method had the characteristics of small calculation delay, high anti-noise ability, and high detection rate. Moreover, the maximum errors of KFF, Random, and PSO were 6.4%, 6.2%, and 5.4%, respectively. The improved method had good estimation accuracy and an excellent global optimization. Meanwhile, the suitable ratio of diameter to current penetration depth, the thickness of crucible wall, and power frequency were beneficial to the improvements in power factor and thermal efficiency. Thus, the finding is helpful as a guide to determining the design of a medium-frequency induction furnace, which may be of interest for improvements in performance under different operating conditions.

Keywords: chaos; immune; chaos immune optimization algorithm; medium-frequency induction furnace

Citation: Zuo, H.; Zhu, Y.; Tan, D.; Cui, S.; Tan, J.; Zhong, D. Investigation on Energy-Effectiveness Enhancement of Medium-Frequency Induction Furnace Based on an Adaptive Chaos Immune Optimization Algorithm with Mutative Scale. *Processes* **2022**, *10*, 491. https://doi.org/10.3390/pr10030491

Academic Editor: Antonino Recca

Received: 5 February 2022
Accepted: 27 February 2022
Published: 28 February 2022

1. Introduction

With the rapid development of industrial technology in the 20th century [1,2], the medium-frequency induction furnace is widely used in the steelmaking industry [3]. Due to the contactless electromagnetic stirring of melt, the medium-frequency induction furnace improves the mixing and chemical homogeneity of metal in the furnace [4]. In the furnace, an oscillating magnetic field produced by the harmonic current heats up the metal. Due to the harmonic nature, the magnetic field can be regulated by the shining effect. In addition, it has been found that the magnetic field produced by the harmonic current is mainly concentrated in a skin layer near the surfaces of the melt [5].

In general, a medium-frequency furnace heating device is a new generation of metal heating equipment [6]. It has the advantages of small volume, light weight, high efficiency, good quality and being favorable for the environment. The medium-frequency furnace is a kind of power-supply device that changes the alternating current into a direct current and

then to a medium-frequency furnace. In the process, many harmonics generate and flow through the power grid, resulting in a decrease in power factor [7]. Harmonic current not only increases the transmission current, resulting in additional losses, but also accelerates the insulation aging of electrical equipment. In addition, the medium-frequency furnace needs to consume a certain amount of reactive power [8]. If the transmission of reactive power is too large, it may reduce the power factor and increase the additional loss of the transmission line. This needs to compensate for the reactive power required by the load, so as to reduce the large amount of reactive power transmitted in the transmission line [9]. The compensation of reactive power at the load side can improve the power factor, which is a very effective measure to reduce the loss [10].

In the steelmaking process, the magnetic losses and thermal effects are important characteristics of a medium-frequency induction furnace [11]. In order to overcome the shortcomings of the traditional static load model, many experts and scholars have put their efforts into how to predict the characteristics of medium-frequency induction furnaces, and many countermeasures have been proposed. For instance, Ref. [12] established the load models of medium-frequency induction furnaces with different load characteristics, and analyzed the effects of different loads of medium-frequency induction furnaces on the power grid. The results showed that the exponent of the power function depends on the ratio of hysteresis loss to eddy current loss and on the number of actively moving domain walls. Ref. [13] developed a medium-frequency induction furnace model and investigated the harmonic characteristics of a medium-frequency furnace. Then, a dynamic filter for the medium-frequency induction furnace was proposed to solve the filtering problem. Now, research on medium-frequency furnaces mainly focuses on the voltage and harmonic characteristics. However, studies on frequency characteristics are few. It was found that the general current frequency would change to a certain extent. The selections of medium-frequency furnace models and parameters are very important to the efficiency of the medium-frequency furnace. Ref. [14] developed a medium-frequency induction furnace model. The results showed that the time-average flow obtained by numerical calculation was in good quantitative agreement with the experimental data. Therefore, the study of medium-frequency furnaces is helpful to reduce losses in the process of transmission and improve the stability of the power system and service life of the equipment.

The artificial immune algorithm has been gradually developed on the basis of the genetic algorithm [15]. The algorithm can simulate the biological immune system to exclude foreign antigens [16,17], and it draws lessons from the characteristics of the human immune system's self-adaptive regulation and self-organizing learning [18]. The method retains the advantages of the genetic algorithm, and can purposefully and selectively use the relevant knowledge and information features in the problem to be solved to suppress the degradation phenomenon caused by some factors in the calculation process [19]. More and more scholars have begun to pay attention to the research, combining the algorithm with the immune algorithm [20], evolutionary algorithm [21], particle swarm optimization algorithm [22], and others [23], to improve the optimization performance of the algorithms. Hong et al. [24] studied the convergence speed of the general artificial immune algorithm using random process theory instead of the eigenvalue estimation of traditional state transition matrix. Simulation results showed the correctness of the estimation method. The estimation method could be used to judge the convergence and convergence speed of a class of artificial immune algorithms. Xu et al. [25] proposed an intelligent terminal test case sequencing algorithm based on the artificial immune algorithm to solve the problems of the traditional genetic algorithm in solving the problem of test case sequencing. The experimental results showed that compared with the genetic algorithm, the algorithm based on the artificial immune algorithm had stronger global search ability and did not easily fall into local optimization, which showed that the artificial immune algorithm was more stable and could better solve the problem of test case sequencing. Miralvand et al. [26] applied the artificial immune algorithm to optimization problems. Comparing the results of this method with other preprocessing methods showed the superiority of this method.

Therefore, in 90% of cases, this method had the best performance based on different metrics. In addition, Panek et al. [27] introduced a new application of model reduction in on-line temperature measurement based on the finite element method. The results showed that more complex, program-controlled, or hybrid strategies need a higher-order MOR model to solve the problem accurately. The proposed four-degree meta model provided sufficiently accurate results, being very fast and able to be implemented in a microcontroller.

The immune algorithm with adaptive parameters, called an adaptive chaotic immune optimization algorithm with mutative scale (ACIOA), is a promising variant of and substantial improvement on the immune algorithm and the chaos algorithm [28]. When the proper values are required to change, or they are not known primarily throughout the stochastic search process [29], the self-adapting parameter strategy is generally used in control parameters [30]. Thus, the control parameter can automatically adapt to the changing environment in the ACIOA [31]. Furthermore, the adapting strategy in the basic chaotic immune optimization algorithm cannot anticipate the possibility of dynamically changing the coefficient values from the variable system according to the feedback in the search process [32]. Thus, the adjustment coefficient should be treated as a self-adapting parameter associated with the current agent performance and the estimated fitness value of each generation [33]. That is to say, based on the relevant theory and feedback mechanism [34], the fitness of the optimal population selected by the best population and selection technique is presented [35,36]. The self-adaptive mechanism and the natural selection strategy are employed to help the chaotic immune optimization algorithm while jumping out of the local optimum trap [37,38]. In order to implement the adaptive scheme of automatic adjustment coefficient, the dynamic feedback mechanism [39], which depends on the adaptive variable scale scheme of the chaotic immune optimization technique, is utilized [40,41]. The good individuals are selected and removed randomly from the population [42]. Conferring with the fitness function, the population is carefully chosen by the tournament selection strategy [43]. The adaptive variable scale algorithm can continuously modify the variable search space, and takes the optimal number of cycles as the control index of the algorithm [44]. However, this algorithm is not superior to all mathematical optimization problems, such as the no free lunch theorem [45,46]. However, in the mathematical optimization problems proposed in this paper, the proposed algorithm is superior to other algorithms.

To overcome the aforementioned shortcomings, in this paper, an ACIOA is proposed based on the immune algorithm and the chaos algorithm, and is used to investigate the medium-frequency induction furnace. In addition, the efficiency parameters of the medium-frequency induction furnace are simulated and optimized using this method. The ACIOA has the fastest convergence speed and the highest iterative accuracy. The self-adapting strategy in automatic adjustment coefficient is introduced and employed to investigate the effects on the performance of the medium-frequency induction furnace of the diameter of the heated cylindrical material, the thickness of the crucible wall, the fullness degree of the induction coil, the ratio of diameter to current penetration depth, and power frequency. It was found that the optimization algorithm can continuously modify the variable search space and take the optimal number of cycles as the control index to carry out the search. Thus, the finding is helpful as a guide to determine the design of a medium-frequency induction furnace, which may be of interest for improvements in performance under different operating conditions.

2. Materials and Methods

An intermediate-frequency furnace with an inverter circuit of hybrid power supply is showed in Figure 1. As shown in Figure 1a, the material with diameter d is heated due to electromagnetic induction after it is put into the inductor (with inner diameter D and outer diameter D_0) and then the two ends of the inductor are connected with an alternating current with frequency f.

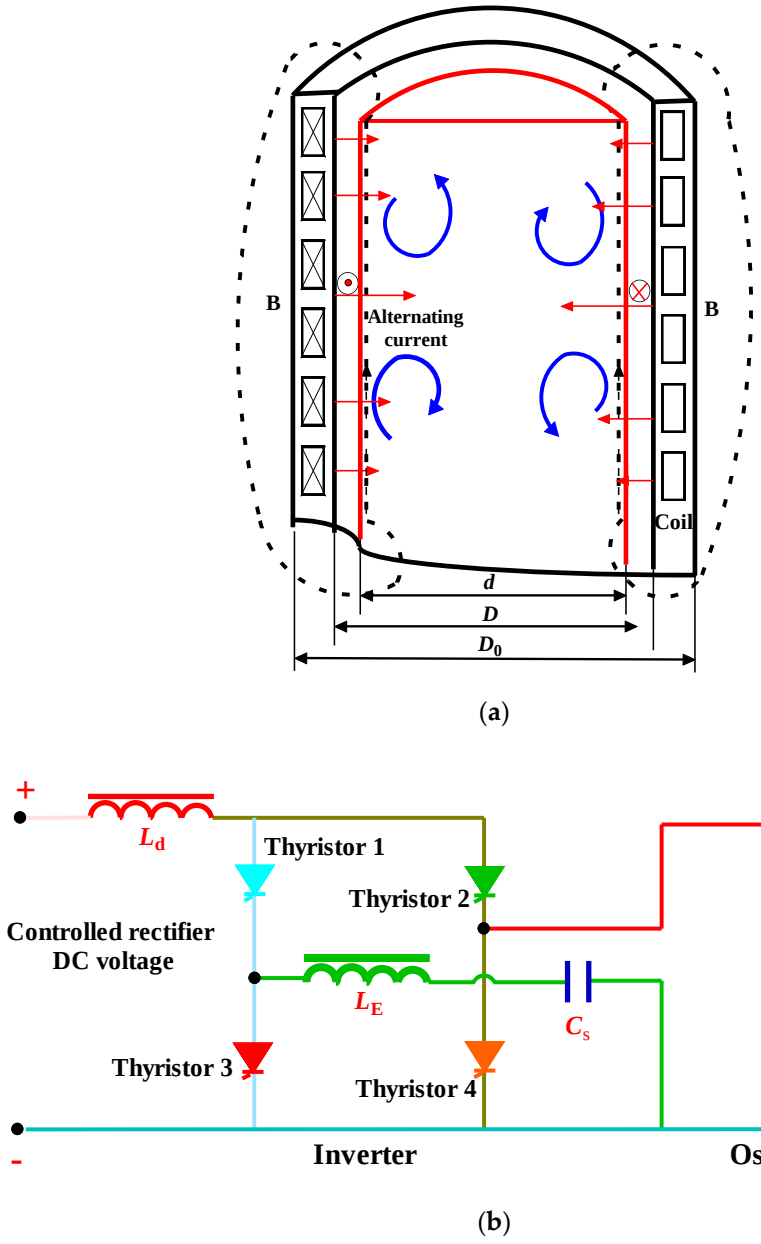

Figure 1. An intermediate-frequency induction furnace with inverter circuit of hybrid power supply. (**a**) structure diagram of intermediate induction frequency furnace; (**b**) inverter circuit of hybrid power supply.

2.1. Energy Effectiveness Optimization Model of Medium-Frequency Induction Furnace

With the development of industry, the medium-frequency induction furnace has been paid more and more attention and has been promoted for its features of metal and alloy melting, heat treatment, and diathermy due to its high efficiency, fast heating, and easy control. However, it is more and more important to evaluate the effectiveness of the intermediate-frequency nonmagnetic period [16]. Therefore, the ACIOA is employed to optimize the electromagnetic efficiency of the intermediate-frequency induction furnace in the paper.

The minimum heating time τ can be calculated by the following equation:

$$\tau = \frac{(d - \delta_{m1})^2}{16\alpha}\left(\frac{t_2 - t_1}{\Delta t} - \frac{1}{2}\right) \quad (1)$$

where d is the diameter of heated cylindrical material, m; α is the thermal conductivity of heating materials, m^2/s; t_1 is the temperature of heating material at the start of constant heat flux, °C; t_2 is the temperature of heating material at the end of constant heat flux, °C; Δt is the maximum allowable temperature difference between central temperature and surface temperature of heating material, °C.

In addition, the current penetration depth in the furnace can be solved by the following equation:

$$\delta_{m1} = 50.3\sqrt{\frac{\rho_{m1}}{\mu_{m1} f}} \tag{2}$$

where ρ_{m1} is the material resistivity, Ω·m; μ_{m1} is the material permeability, H/m; f is the heating power frequency, Hz.

The effective power can be calculated by the following equation:

$$P_{\mu 1} = \frac{N \cdot m \cdot c_1(t_2 - t_1)}{\tau} \tag{3}$$

where N is the number of heating materials; m is each material mass, kg; c_1 is the material specific heat capacity, J/(kg·°C).

The heat loss of the intermediate-frequency induction furnace at the outlet of heater is calculated by the following equation:

$$P_{d1} = \varepsilon \cdot \sigma_0 \cdot (t_2 + 273)^4 \cdot S_1 \tag{4}$$

where ε is the material surface blackness; σ_0 is the Stephen Boltzmann constant, $\sigma_0 = 5.67 \times 10^{-8}$ W/(K^4·m^2); S_1 is the radiating area at outlet, $S_1 = \pi \cdot d^2/4$, m^2.

The loss of heat conduction at the outlet of heater is calculated as follows:

$$P_{d2} = \frac{\lambda_2}{\delta}(t_m - t_0)S_2 \tag{5}$$

where λ_2 is the thermal conductivity of induction coil insulation layer, W/(m·°C); δ is the thermal insulation layer, m; t_m is the average temperature of constant heat flux, $t_m = (t_1 + t_2)/2$, °C; S_2 is the induction coil area, m^2; t_0 is the cooling water temperature, °C.

As mentioned above, the total heat loss power can be expressed as:

$$P_d = P_{d1} + P_{d2} + P_{d3} \tag{6}$$

where P_{d3} is the radiation heat loss, W.

The magnetization force of inductor can be calculated by the following equation:

$$I_n^2 = \frac{500(P_{\mu 1} + P_{d1})}{\sqrt{\rho_{m1} \cdot \mu_{m1} \cdot f} \cdot S_m \cdot k_{am1} \cdot k_t} \tag{7}$$

where k_{am1} is the active power correction coefficient; S_m is the surface area of absorbed electromagnetic energy, m^2; k_t is the effect coefficient.

The inductor is made of copper tube, which is cooled by water at t_0 °C. The reactive power in the working process can be calculated by the following equation:

$$P_{cm1} = 2.0 \times 10^{-3} I_n^2 \sqrt{\rho_{m1} \mu_{m1} f} \cdot S_m \cdot k_{cm1} \cdot k_t \tag{8}$$

where k_{cm1} is the reactive power correction coefficient.

The active power of the inductor can be calculated by the following equation:

$$P_{ac} = 2.0 \times 10^{-3} I_n^2 \sqrt{\rho_c f} S_c k_{ac} k_t k_s^{-1} \tag{9}$$

where k_{ac} is the active power correction coefficient; ρ_c is the resistivity of inductor, Ω·m; S_c is the inner surface area of inductor, m^2; k_s is the fullness of induction coil.

The active power correction coefficient can be calculated by the following equation:

$$k_{ac} = \frac{2fb}{503\sqrt{\rho_c/(u_c f)}} \tag{10}$$

where μ_c is the relative permeability of inductor.

The reactive power of the inductor can be calculated by the following equation:

$$P_{rc} = 2.0 \times 10^{-3} I_n^2 \sqrt{\rho_c f} S_c k_{rc} k_t k_s^{-1} \tag{11}$$

where k_{rc} is the reactive power compensation coefficient; R is the inner radius of inductor, m.

The reactive power correction coefficient can be calculated by the following equation:

$$k_{rc} = \frac{f\sqrt{2}R}{503\sqrt{\rho_c/(u_c f)}} \tag{12}$$

The clearance reactive power of inductor can be calculated by the following equation:

$$P_{rg} = 6.20 \times 10^{-6} I_n^2 \cdot f \cdot L(d_g^2 - d^2)k_t \tag{13}$$

Total active power in the nonmagnetic period can be calculated by the following equation:

$$P_{a1} = P_{\mu 1} + P_{d1} + P_{ac} \tag{14}$$

Total active power in the magnetic period can be calculated by the following equation:

$$P_{r1} = P_{rm1} + P_{rc} + P_{rg} \tag{15}$$

The apparent power in the nonmagnetic period can be calculated as follows:

$$P_{01} = \sqrt{P_{a1}^2 + P_{r1}^2} \tag{16}$$

Then, the power factor cos φ in the nonmagnetic period can be calculated as follows:

$$\cos\varphi = P_{a1}/P_{01} \tag{17}$$

The electrical thermal effective in the nonmagnetic period can be calculated as follows:

$$\eta_1 = \eta_{e1} \cdot \eta_{t1} = \frac{P_{\mu 1} + P_{d1}}{P_{a1}} \times \frac{P_{\mu 1}}{P_{d1} + P_{u1}} \tag{18}$$

In this work, a medium-frequency induction furnace with a length of 700 mm was investigated, in which process, three steel blanks were heated. The length of the induction coil of electric furnace was 650 mm; the inner diameter of coil was 130 mm; the thickness of guard plate at both ends was 50 mm; the thickness of the insulation layer was 20 mm. In addition, there were three triangle shaped heat-resistant steel pipes with the diameter of 20 mm in the induction furnace, one of which was used as the limit rail, while the others were used for the blank pulley. In the process of non-magnetic heating, the temperature of the heated cylindrical material was heated from 800 °C to 1200 °C, and the maximum temperature difference between the center and the surface was 100 °C. The thermal effective of the induction furnace η_1 is important, and it directly reflects the economic efficiency of the induction furnace. Thus, the optimization of the thermal effective η_1 of the medium-frequency induction furnace is to solve the global maximum optimization problem. The objective function selected in the process of optimization is shown as follows:

$$\begin{cases} \max \eta_1(f,d) \\ \quad a_1 \le f \le b_1 \\ \quad a_2 \le d \le b_2 \end{cases} \tag{19}$$

where d is the diameter of heated cylindrical material; f is the power frequency.

Thus, the one-dimensional self-mapping can be defined as follows:

$$\begin{cases} x_{n+1} = \sin(2/x_n) & n = 0,\ 1,\ 2,\ \cdots, N \\ -1 \le x_n \le 1 & x_n \ne 0 \end{cases} \tag{20}$$

2.2. An Adaptive Mutative-Scale Chaos Immune Optimization Algorithm

In general, the artificial immune algorithm always uses the evolutionary algorithm or matching algorithm to achieve the purpose of data training and immune memory. According to the research experience of previous scholars, the evolutionary algorithm has a better adaptive performance than the matching algorithm [47]. Therefore, the evolutionary algorithm with the better adaptability was employed to carry out the next research work in the paper. The main steps of the chaotic immune clustering algorithm are as follows:

Step 1: Distinguishing and input of antigens $\{Ag\}$. According to Equation (20), the chaotic variables of random initialization antibody $\{Ag\}$ can be generated within the finite region (0, 1). In addition, the random variables of the input antigen are standardized.

Step 2: Each antigen is defined in turn according to the different requirements.

Step 2.1: The affinity of each antibody and antigen should be calculated by the following Equation (21) in turn.

$$a_{ij} = \left(\sum_{k=1}^{n} (Ab_{ik} - Ag_{jk})^2 \right)^{1/2} \tag{21}$$

where a_{ij} is the affinity; Ab_i is the antibody; Ag_j is the antigen.

Step 2.2: The occurrence of cell differentiation. Antibodies with the highest affinity with the antigen are selected as the differentiated cells of the memory network.

Step 2.3: The antibodies with the high affinity are cloned. In general, excellent network cells with the highest affinity will clone more cells N_c.

Step 2.4: The mutation operation is carried out by the cloned cells. The equation can be expressed as:

$$C = C - \alpha(C - X) \tag{22}$$

where C is the cloned antibody; X is the antigen cell; α is the mutation rates.

Step 2.5: If the number of cloned cells is not enough, the affinity of the cloned antibody is recalculated according to Step 2.1. The excellent mutation network cells are selected as the data set of the memory cell (M_p).

Step 2.6: The similarity of each antibody should be calculated by the following equation. When the similarity of the antibody is less than the value domain (δ_s), the antibody is selected in the data set of the memory cell (M_p). The similarity of antibody s_{ij} can be calculated by the following equation:

$$s_{ij} = \left(\sum_{k=1}^{n} (Ab_{ik} - Ag_{jk})^2 \right)^{1/2} \tag{23}$$

Step 3: A new memory data set (M) is obtained by combing the data set of the memory cell (M_p) and memory data set.

Step 4: Select good individuals and carry out chaos search. Suppose that the excellent individual is ζ and the chaos search is carried out. The reduction in search range can be calculated by the following equation:

$$\begin{cases} a_i' = \xi_i - \phi(b_i - a_i) \\ b_i' = \xi_i - \phi(b_i - a_i) \end{cases} \tag{24}$$

where φ is constriction factor, the clearance is in the region of (0, 0.5).

In order to prevent the calculated value from crossing the value range, the following assumptions should be made. If $a_i' < a_i$, then $b_i' < b_i$; on the contrary, if $a_i' > a_i$, then $b_i' = b_i$.

The vector of the excellent individuals selected in the new area can be expressed as:

$$Y_i = \frac{\xi_i - a_i'}{b_i' - a_i'} \tag{25}$$

The new chaotic variable is formed by the linear combination of vector and individual. In addition, an automatic adjustment coefficient β_i ($0 < \beta_i < 1$) is introduced and employed to search.

Thus, the new search can be expressed as:

$$\xi_{i,n+1}' = (1 - \beta_i)Y_i + \beta_i \xi_{i,n+1} \tag{26}$$

The automatic adjustment coefficient can be determined by the following equation:

$$\beta_i = 1 - \left(\frac{K-1}{K}\right)^m \tag{27}$$

where m is an integer, and K is the number of iterations.

Step 5: In order to improve the convergence speed of calculation, some individuals can be selected to replace the individuals with poor affinity, according to Equation (20). Then return to Step 2 until network convergence, when the network size and cell distance mean change little or remain unchanged.

2.3. Astringency of Adaptive Mutative-Scale Chaos Immune Optimization Algorithm

The adaptive chaos immune optimization algorithm with mutative scale belongs to the descent algorithm. In the process of calculation, the algorithm can overcome the failure of the chaotic algorithm and make up for its shortcomings. Thus, its accuracy is better than that of the immune algorithm. In addition, the algorithm shows a good convergence. Firstly, it is assumed that R_0 is the neighborhood of global optimal solution ζ^*. Secondly, the sequences ζ_i generated by the optimization algorithm of adaptive variable scale chaotic immune is the set A_i in the neighborhood of global optimal solution. It can be found $A_1 \subset A_2 \subset \cdots A_i \subset \cdots$. The probability measure is monotonically decreasing. Finally, the $P(A_i) \leq 1$ can be expressed as:

$$\lim_{i \to \infty} P(A_i) = P(\overset{\infty}{\underset{i=1}{\cup}} A_i) = 1 \tag{28}$$

An arbitrary positive number θ is selected in the finite region (0, 1). Then, there is a positive number N. When the $n > N$, there is $P(A_N) \geq 1 - \theta, P(\overline{A_N}) < \theta$. Thus, it should be satisfied with $P(\overline{A_n}, n > N) \leq \varepsilon^{i-N}$. If n is large enough, the algorithm can obtain the global optimal solution with 100% probability.

2.4. Optimization Algorithm Validation

Each node mainly consists of two functions: one is to transmit data, while the other is to act as the routing function of other nodes in Mobile Ad Hoc Networks (MANETs). The routing from each node to other nodes mainly depends on all nodes participating in the connection in the system. In general, the network attacks are very common in routing protocols for MANETs. Therefore, taking an example for Ad Hoc on Demand Distance Vector Routing (AODV) protocol in the paper, it mainly considers two typical Dos attacks (FFRR and black hole). In the process of an FFRR attack, the malicious nodes will produce many ROUTE_RE_QUESTs, then many network resources and significant amounts of broadband are occupied, resulting in failure. In addition, in the process of a black hole attack, a malicious node that has the shortest and best path broadcasts to other nodes around it, then continuously sends ROUTE_REQUEST, which will eventually

capture the whole network, resulting in failure. This is akin to forming a black hole that only absorbs data.

The MANETs anomaly detection system is very complex. Each node and its adjacent nodes have their own characteristics. For instance, there are more than 100 features related to traffic alone in the AODV routing protocol. In order to reduce the computation load and time, four features of DoS attack are selected and employed to analyze. The traffic characteristics of adjacent nodes are shown in Table 1. In the calculation process, the 10-folder cross validation method is used to segment, train, and detect the data, and then the average value is taken as the final value.

Table 1. Traffic characteristics of adjacent nodes.

Item	Detailed
NBRecv	Number of data accepted by adjacent nodes
NBSent	Number of data sent by adjacent nodes
NBRrepSent	The number of RREQ packets accepted by adjacent nodes
NBRreqSent	The number of RREQ packets sent by adjacent nodes

In the paper, the ns^2 2.3.0 simulation platform of a network attack was employed to investigate the optimization algorithm of adaptive variable scale chaotic immune in the AODV routing protocol. In addition, the simulation time was 800 s in the calculation process. Generally, the intrusion detection performance can be evaluated by detection rate. The simulation was carried out, and Figure 2 shows the detection rates of ACIOA, the RANDOM algorithm, and the particle swarm optimization (PSO) algorithm when noise data and training data sets are 10% and 100, respectively. It can be observed that the improved ACIOA had the fastest convergence speed and the highest iterative accuracy. Moreover, the optimization algorithm can significantly improve the computational efficiency and reduce the calculation time. Thus, the improved adaptive chaotic immune optimization algorithm has obvious advantages.

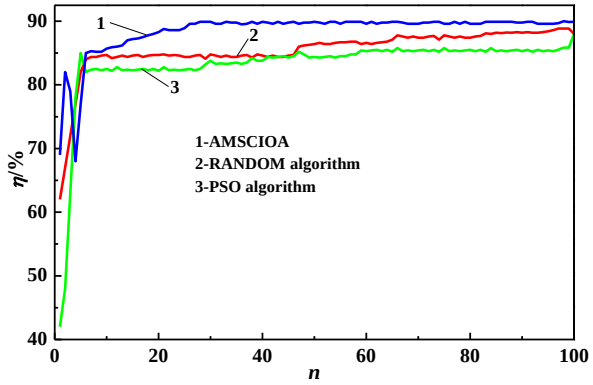

Figure 2. The detection rates (Noise level is 10%).

2.5. Validation of the Model and Methods

In this paper, the ACIOA was used to optimize the medium-frequency induction furnace. The results of optimization and non-optimization are shown in Table 2, respectively. In general, the active power, total heat loss power, and excessive clearance reactive power ere the main reasons for the decrease in power factor and thermal effective of the induction furnace. It can be seen that the system power factor and thermal effective of the induction furnace in the frequency domain were better than before. When the diameter of heated cylindrical material was 103 mm and the power frequency, the power factor and thermal effective were greatly improved. For instance, the power factor increased from 0.156 to 0.400, and thermal effective increased from 54.7% to 77.2%.

Table 2. Comparison of medium-frequency induction furnace parameters in the non-magnetic period.

Item	*T*/s	*D*/mm	*F*/Hz	$P_{\mu 1}$/kW	P_{a1}/kW	P_{r1}/kVar	η_1/%
Before optimization	100	71	10^3	50.7	92.6	578.1	54.7
After optimization	110	104	1151	64.4	119.4	273.1	77.2

3. Results and Discussion

3.1. Energy Effectiveness Analysis on Medium-Frequency Induction Furnace

3.1.1. Power Analysis

As for the heating process of the intermediate-frequency induction furnace, the active power P_a of induction heating can be expressed as follows:

$$P_a = P_{am} + P_{ac} = P_u + P_d + P_{ac} \tag{29}$$

where P_{am} is the active power of the material, $P_{am} = {I_m}^2 R_m$, W; I_m is induced current of the material, A; R_m is the resistance of material, Ω; P_{ac} is the active power of the induction coil, W; $P_{ac} = {I_c}^2 R_c$, W; I_c is induced current of induction coil, A; R_c is the resistance of induction coil, Ω; P_u is useful power for heating the material, W; P_d is heat loss power for heating the furnace wall and the atmosphere, W.

On the other hand, since the induction coil (inductor L_1) and material (inductor L_2) are energy storage elements, electric energy should be stored when the current flows. This part of power is called reactive power P_r. The magnetic force line generated by the induction coil does not cut the material in the gap between the material and the induction coil, and the reactive power P_r of induction heating is expressed as follow:

$$P_r = P_{rm} + P_{rg} + P_{rc} \tag{30}$$

where P_{rm} is the reactive power of the furnace burden, W; P_{rg} is the reactive power of the gap, W; P_{rc} is the reactive power of induction coil, W.

3.1.2. Electrothermal Efficiency Analysis

The thermal efficiency of the medium-frequency induction furnace is related to the gap between the inductor and the material, the ratio of material diameter to current penetration depth, and the thermal conductivity of the material, and the value range of its thermal efficiency η_r usually meets η_r = 0.7~0.9.

The research shows that the electric efficiency of the medium-frequency induction furnace is related to the gap between the material and the inductor, the inter turn gap among the inductors, the depth of current penetration, and so on. Under ideal conditions, its electrical efficiency η_d is of a limit electrical efficiency, namely:

$$\eta_d = \frac{1}{1 + \sqrt{\rho_c / (\rho_m \mu_m)}} \tag{31}$$

where ρ_c and ρ_m are resistivity of inductor and material, respectively, Ω·m; μ_m is relative permeability of material.

For water-cooled steel sensors, resistivity ρ_c of the inductor is a fixed value, so the electrical efficiency depends on the nature of the material. Electrothermal efficiency η of the medium-frequency induction furnace is the product of its electrical efficiency η_d and thermal efficiency η_r, namely, $\eta = \eta_d \cdot \eta_r$. There is a contradiction between electrical efficiency η_d and thermal efficiency η_r. For example, increasing the thickness of the insulation layer is conducive to improving the thermal efficiency η_r, but ratio increase of D/d (D is the inner diameter of the inductor and d is the diameter of the furnace burden) will reduce the electrical efficiency η_d. Moreover, increasing the power supply frequency is conducive to improving the electrical efficiency, but reduces the thermal efficiency. Therefore, compromise conditions should be created to obtain higher electrothermal efficiency. Generally, industrial production does not allow the electric heating efficiency to be lower than 0.5.

As shown in Figure 3, there is a close relationship between electrothermal efficiency and the ratio of d/δ_m (δ_m is the current penetration depth). The ratio increase of d/δ_m will increase the electrical efficiency and decrease the thermal efficiency. When $d/\delta_m < 5$, the electric efficiency will change greatly, and the change is not obvious later.

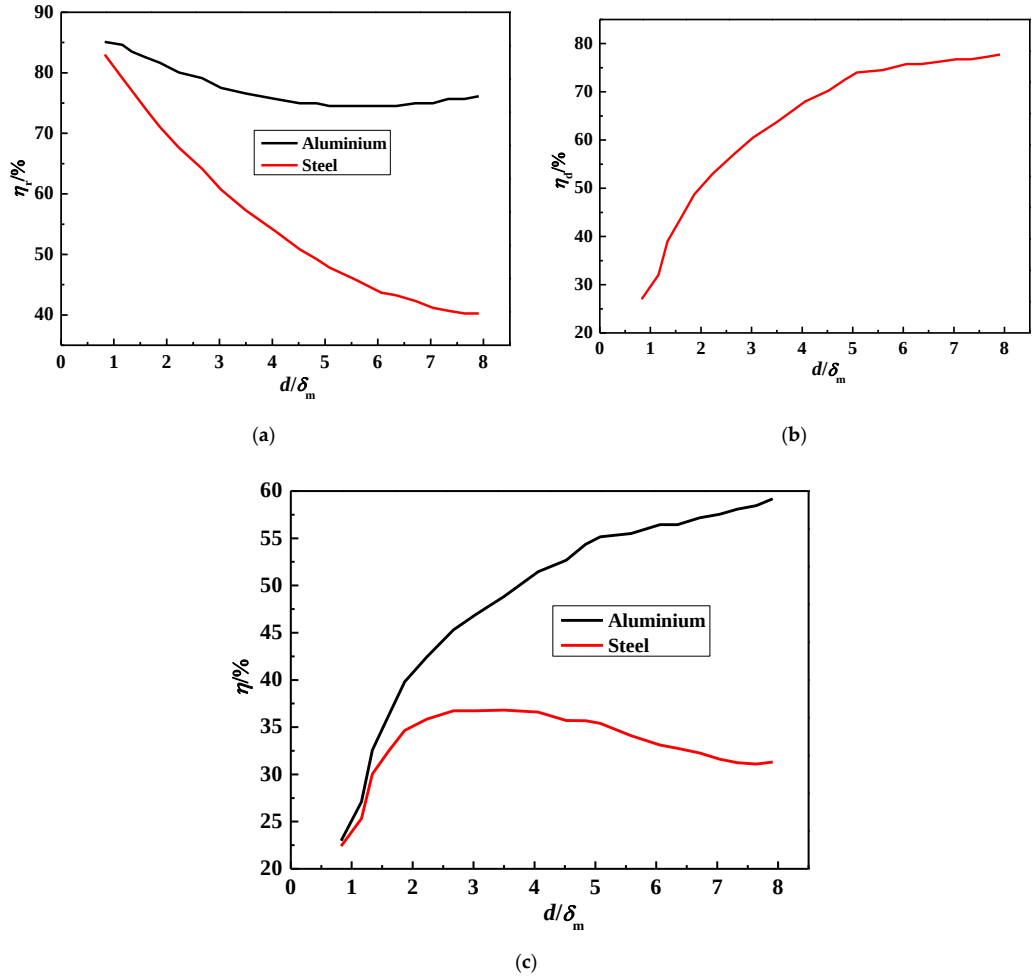

Figure 3. Thermal efficiency, electrical efficiency, and electrothermal efficiency of the medium-frequency induction furnace. (**a**) thermal efficiency η_r; (**b**) electrical efficiency η_d; (**c**) electrothermal efficiency η.

(1) As for material (such as aluminum) with small heat loss, low heating temperature, high thermal conductivity, and low absorption capacity, its thermal efficiency is high and the thermal efficiency change is small. In this case, the electrothermal efficiency mainly depends on the electrical efficiency, and the electrical efficiency is close to the maximum when d/δ_m is equal to 5.

(2) As for material (such as steel) with large heat loss, high heating temperature, low thermal conductivity, and large absorption capacity, its thermal efficiency is low and thermal efficiency changes greatly. In this case, the electrothermal efficiency has a peak value. For cylindrical steel, the corresponding ratio of d/δ_m is about 3.5.

3.1.3. Power Factor Analysis

The power factor of the medium-frequency induction furnace can be expressed as follows:

$$\cos\varphi = \frac{R}{Z} = \frac{P_a}{P_0} = \frac{P_{am} + P_{ac}}{\sqrt{(P_{am} + P_{ac})^2 + (P_{rm} + P_{rc} + P_{rg})^2}} \quad (32)$$

Equation (32) shows that the maximum power factor cosφ of the medium-frequency induction furnace is equal to 0.707 under ideal conditions (active power and reactive power are equal), which is called the ideal power factor. Generally, for a material with infinite size that is closely configured with the inductor, its active power is equal to reactive power, and the power factor is $1/\sqrt{2}$ when it is heated by the medium-frequency induction furnace.

Figure 4 shows the power factor of the medium-frequency induction furnace under induction heating of infinite cylinder. As shown in Figure 4, the biggest impact of the D/d (namely the gap between the material and the inductor) is usually on the cosφ. Moreover, the $\sqrt{2}d/\delta_m$ (namely, the relative thickness of material in current penetration direction) has a significant impact on the cosφ. Generally, the smaller the gap is, the higher the value of the cosφ is, and the value of the cosφ changes due to the change in $\sqrt{2}d/\delta_m$, and its value is of the maximum when $\sqrt{2}d/\delta_m$ is about 3. Therefore, in order to enhance the value of the cosφ, the gap should be reduced as much as possible and the power frequency should be selected appropriately.

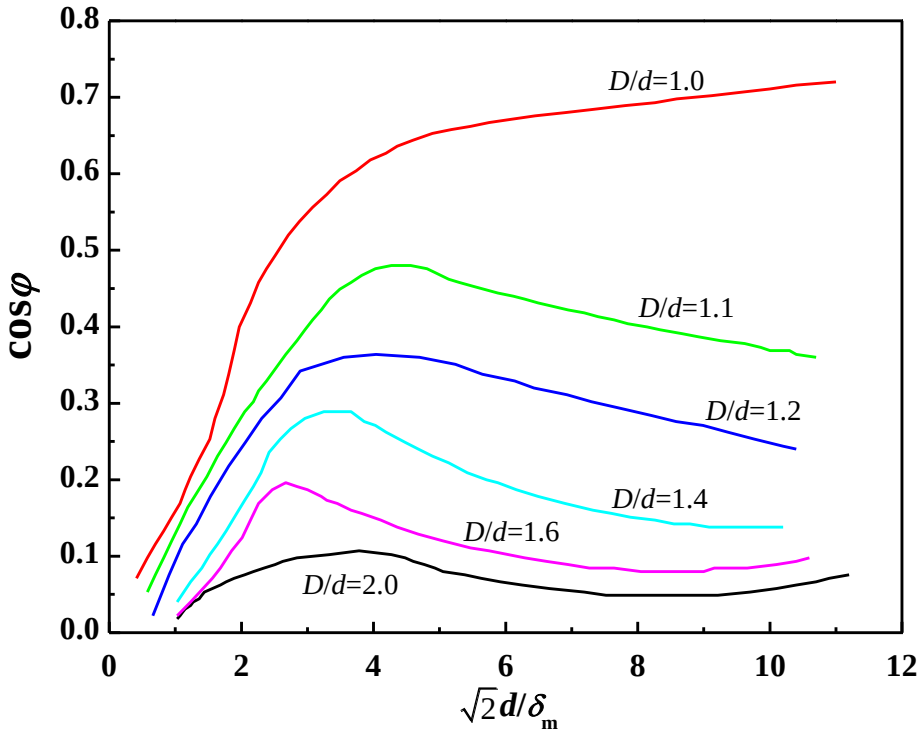

Figure 4. Power factor of the medium-frequency induction furnace under induction heating of infinite cylinder.

3.2. Effect Analysis on Energy-Effectiveness Enhancement of Medium-Frequency Induction Furnace

In this section, the ACIOA is used to optimize the medium-frequency induction furnace. In addition, a comparison between the Kernel Farthest-First (KFF) algorithm, the RANDOM algorithm, ACIOA, and the particle swarm optimization (PSO) algorithm are conducted, and the applicability verification of the selected features is also carried out.

3.2.1. Diameter of Heated Cylindrical Material

The effect of the diameter of heated cylindrical material on circuit performance parameters was shown in Figure 5. It can be seen that the optimal power frequency of electric furnaces decreases with the increase in the diameter of heated cylindrical material when the ratio of diameter to current penetration depth is constant. Moreover, the optimal thermal efficiency decreases slightly with the increase in the diameter of the heated cylindrical material. When the power frequency is appropriate, higher thermal effectiveness and power

factor can be obtained, and the difference is not obvious. Nevertheless, with the increase in the diameter of the heated cylindrical material, the input power of the inductor increases correspondingly. However, the optimal power factor and input power increase with the increase in the diameter of the heated cylindrical material. In addition, it can be observed that the error of the improved method is the smallest and closest to the real value. For instance, the maximum error of the improved method is 4% in Figure 5a. However, the maximum errors of KFF, Random, and PSO are 6%, 7.2%, and 7.8%, respectively. This is due to the fact that the ACIOA has excellent global optimization and rapid convergence. Overall, the proposed method indicates that it has good estimation accuracy in the same and different working conditions of the training set. Esfahani et al. [48] have similar conclusions.

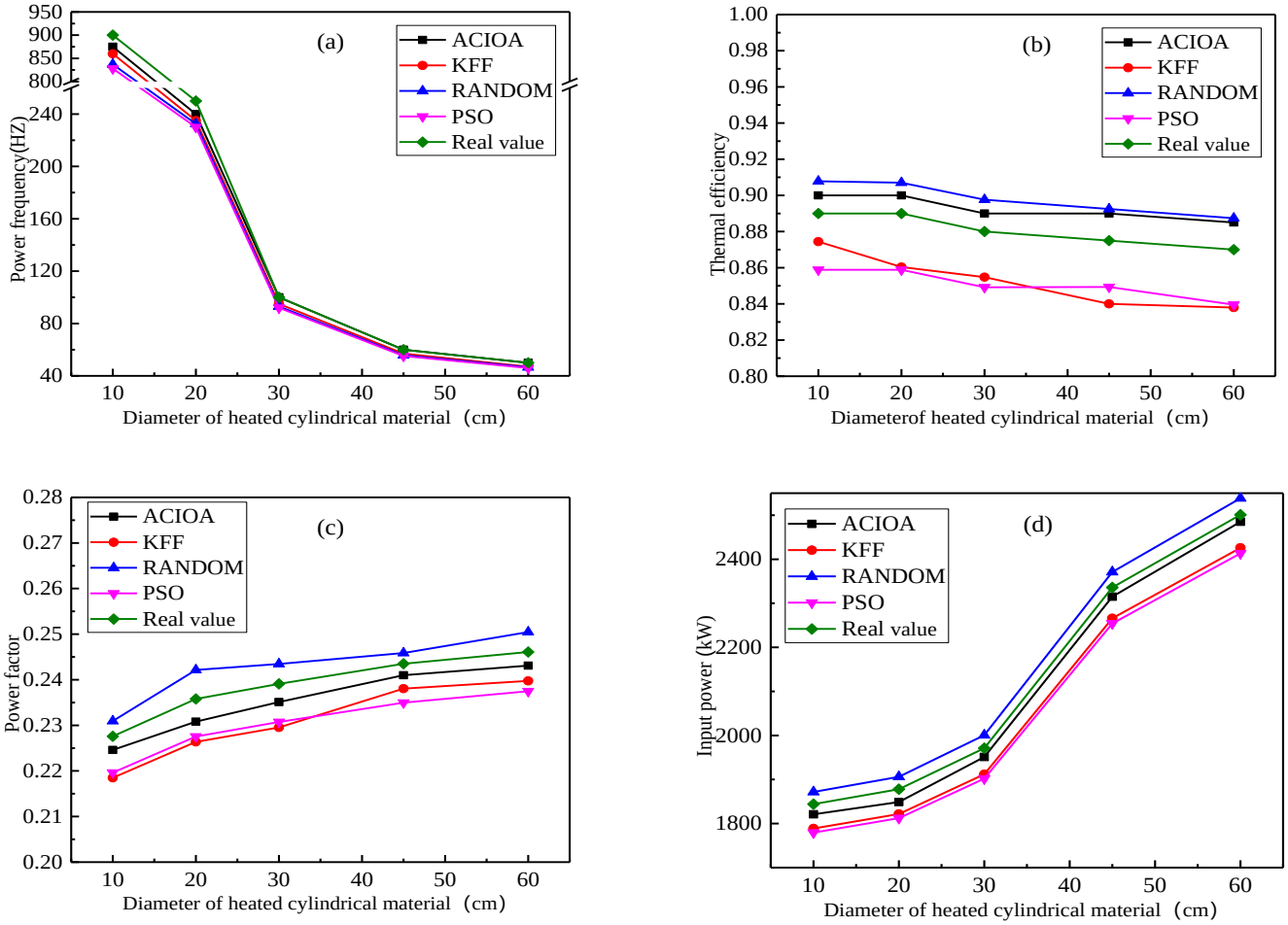

Figure 5. Effect of diameter on circuit performance parameters. (**a**) power frequency; (**b**) thermal efficiency; (**c**) power factor; (**d**) input power.

3.2.2. Thickness of Crucible Wall

The effect of thickness of the crucible wall on circuit performance parameters is shown in Figure 6. It can be observed that the side-wall heat loss decreases with the increase in thickness of the crucible wall. In addition, with the increase in the thickness of the crucible wall, the thermal efficiency increases slightly, and the power factor decreases. The optimal input power firstly decreases and then increases with the increase in thickness of the crucible wall. This is due to the fact that the increased wall thickness of the crucible improves the heat-preservation effect of the furnace. Similarly, the thermal efficiency improves to some extent. In addition, the required input power is not significantly reduced, because the heat loss of the crucible side wall accounts for a small proportion of the required power. Moreover, the increasing thickness of the crucible wall increases the clearance between the

inductor and the crucible, resulting in a sharp drop in power factor. Thus, it is not enough to emphasize one side, but it should be considered synthetically from the whole angle. Tkacheva et al. [49] have similar conclusions.

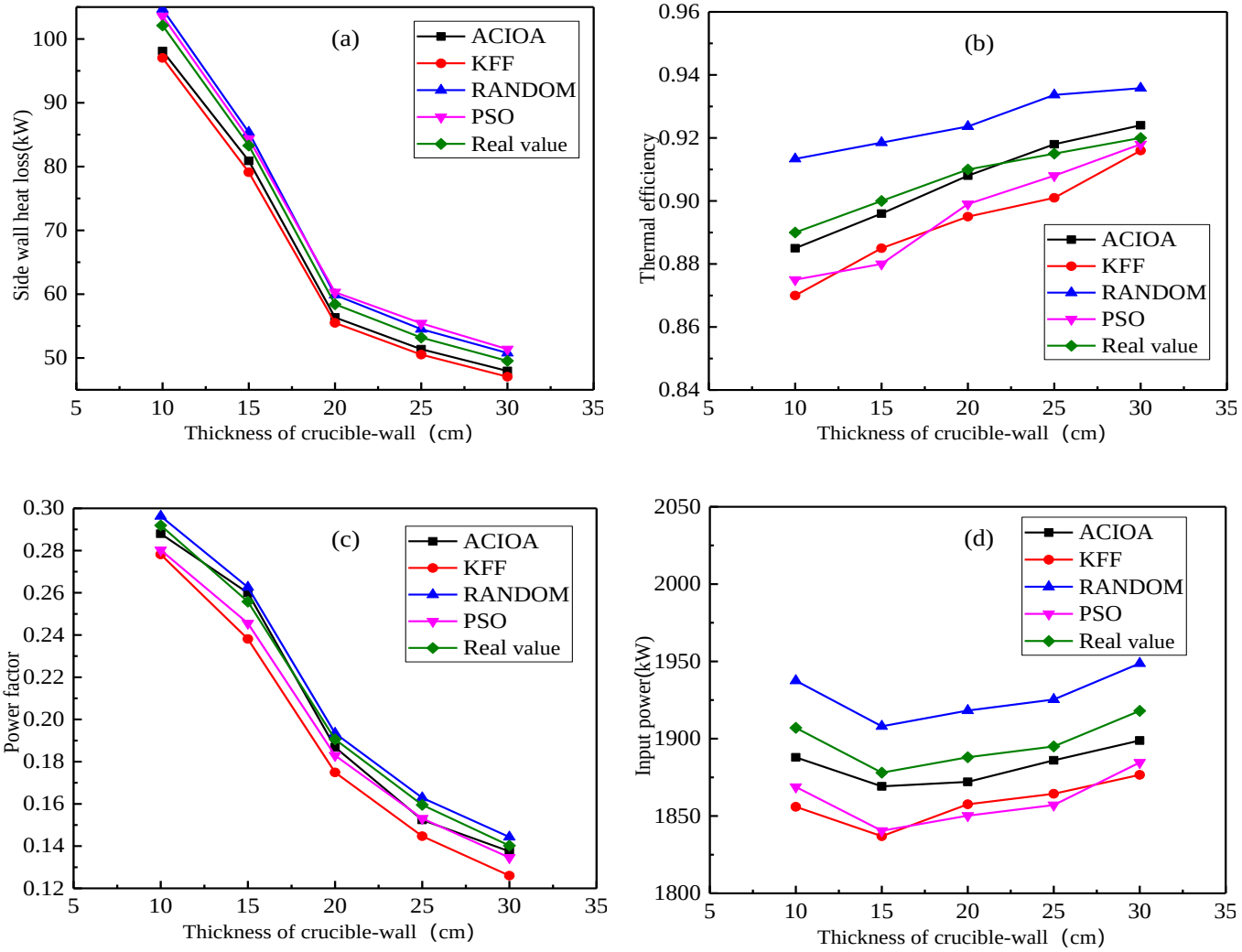

Figure 6. Effect of thickness of crucible wall on circuit performance parameters. (**a**) side-wall heat loss; (**b**) thermal efficiency; (**c**) power factor; (**d**) input power.

In addition, the analysis shows that the improved model can better forecast the operating parameters of the medium-frequency induction furnace. For instance, the maximum error of the improved method is 2% in Figure 6d. However, the maximum errors of KFF, Random, and PSO are 6.4%, 6.2%, and 5.4%, respectively. This is due to the fact that the ACIOA has excellent global optimization and rapid convergence. Similarly, the improved method has good estimation accuracy and excellent global optimization.

3.2.3. Fullness Degree of Induction Coil

The effect of the fullness degree of the induction coil on circuit performance parameters was shown in Figure 7. It showed that the thermal efficiency increased with the increase in the fullness degree of the induction coil. In addition, with the increase in fullness degree of the induction coil, the power factor firstly increases, then decreases, and finally increases. The greater the fullness of the inductor, the smaller the clearance between turns. Thus, greater fullness of the inductor can reduce the power loss and improve the thermal efficiency. With the increase in fullness of the induction coil, the increasing trend of the power factor gradually slows down. In the design process, the fullness of the inductor

should be as large as possible, in order to reduce the clearance between turns. In addition, the analysis shows that the improved model can better predict the operating parameters of the medium-frequency induction furnace.

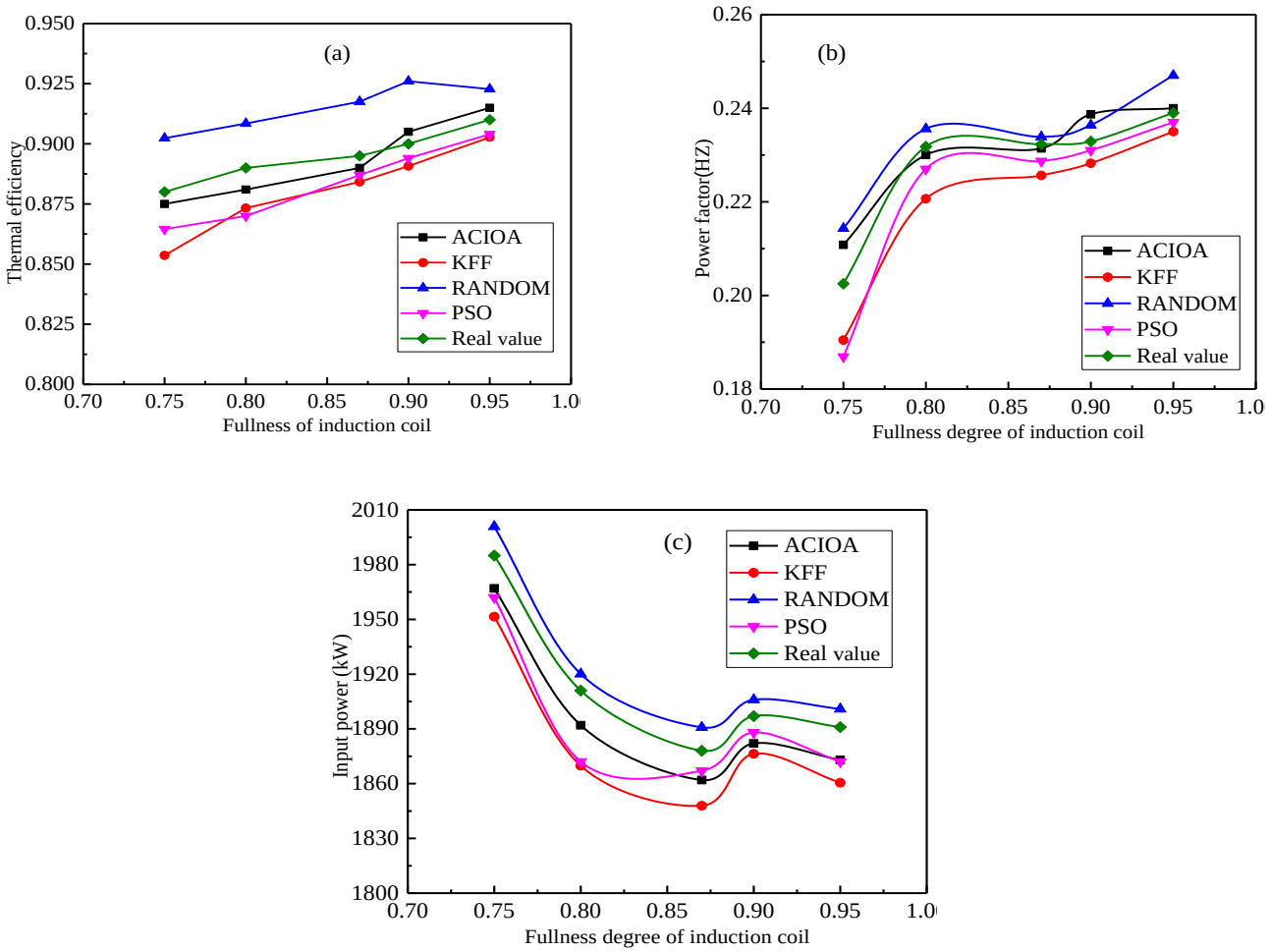

Figure 7. Effect of fullness of induction coil on circuit performance parameters. (**a**) thermal efficiency; (**b**) power factor; (**c**) input power.

3.2.4. Ratio of Diameter to Current Penetration Depth

The effect of the ratio of diameter to current penetration depth on circuit performance parameters is shown in Figure 8. It shows that the power frequency and thermal efficiency increased with the increase in the ratio of diameter to current penetration depth. The input power firstly decreases, then increases, and finally decreases with the increase in the ratio of diameter to current penetration depth. It can be seen that it is very important to choose the appropriate ratio of diameter to current penetration depth. If the penetration depth is too small, the heating time becomes longer and the heat loss increases, which seriously reduces the thermal efficiency and power factor. When the problem becomes more serious, it may even happen that the temperature does not change in the heating process. However, when the penetration depth is too large, the thermal efficiency reduces markedly and the electric efficiency increases slightly. Thus, the thermal efficiency can be improved by increasing power frequency. The increase in power frequency will lead to an increase in production cost. Generally, the suitable ratio of diameter to current penetration depth is between 3.5 and 6.0. Similarly, the analysis shows that the improved model can better predict the operating parameters of the medium-frequency induction furnace. Dou et al. [50] have similar conclusions.

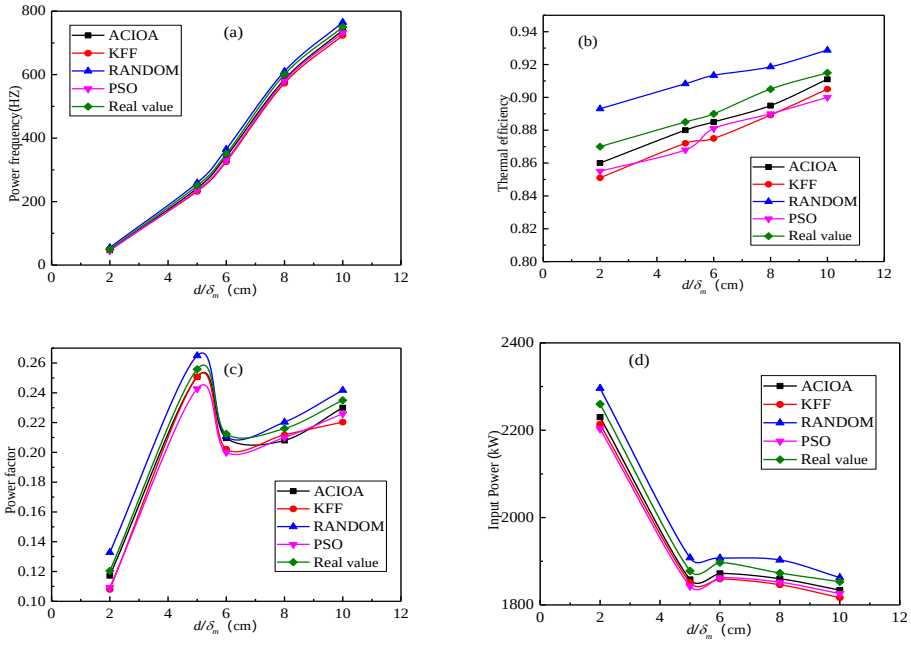

Figure 8. Effect of ratio of charge diameter to current penetration depth on circuit performance parameters. (**a**) power frequency; (**b**) thermal efficiency; (**c**) power factor; (**d**) input power.

3.2.5. Power Frequency

The effect of power frequency on circuit performance parameters is shown in Figure 9. It shows that the current penetration depth decreased with the increase in power frequency, and the thermal efficiency increased with the increase in power frequency. It can be seen that high power frequency is beneficial to the improvements in power factor and thermal efficiency. If the power frequency is too high, it will reduce the power factor and increase the production cost. Thus, a suitable power frequency can effectively improve the power factor and reduce the required power. In the design process, the suitable power frequency should be considered. Only in this way can we save resources and improve efficiency. In addition, the analysis also shows that the improved model can better predict the operating parameters of the medium-frequency induction furnace.

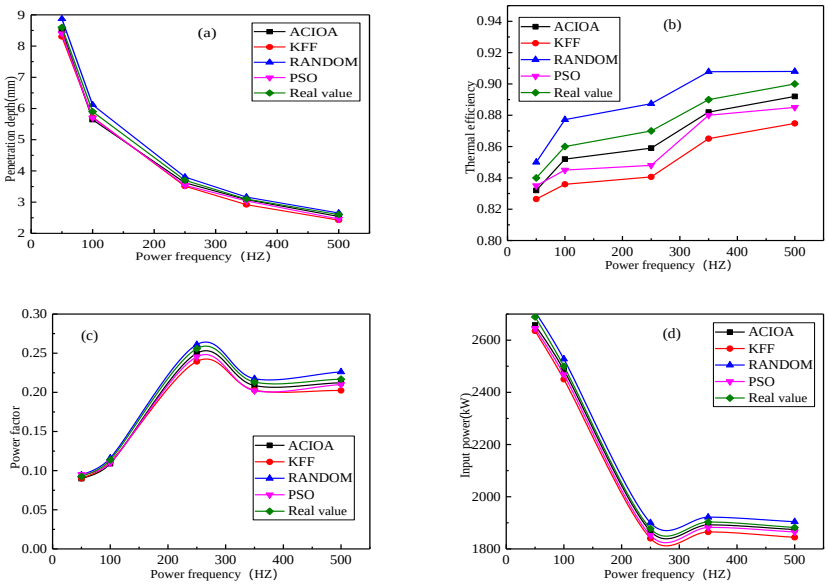

Figure 9. Effect of power frequency on circuit performance parameters. (**a**) power frequency; (**b**) thermal efficiency; (**c**) power factor; (**d**) input power.

As mentioned above, the ACIOA can use efficiency parameters to evaluate the efficiency index of the medium-frequency induction furnace, and has very important engineering value for improving the work efficiency of medium-frequency induction furnaces. Thus, the effect shows that the optimization algorithm is an accurate and fast block-matching search algorithm.

4. Conclusions

Because of the increasing energy crisis [51–58] and environmental pollution [59–68], it was investigated how to enhance energy-effectiveness of medium-frequency induction furnace using ACIOA in this study. In the case of MANETs intrusion, three test functions were analyzed and optimized using the ACIOA algorithm. In addition, the efficiency parameters of the medium-frequency induction furnace were simulated and optimized using this method. The main conclusions are as follows:

(1) Due to the good global optimization and fast convergence of ACIOA, the improved method has the smallest error and is closest to the actual value. In addition, the method has good estimation accuracy for both similar and different operating conditions of the training set.
(2) The optimization algorithm can continuously modify the variable search space and take the optimal number of cycles as the control index to carry out the search. It can reduce the influence of noise on the performance of the intrusion systems.
(3) Because the increase in crucible wall-thickness improves the insulation of the furnace, the optimal input power is first reduced and then increased. Again, the improved method has good estimation accuracy and global optimization capability.
(4) The suitable ratio of diameter to current penetration depth is between 3.5 and 6.0, and is beneficial to the improvements in power factor and thermal efficiency. The side-wall heat loss decreases with the increase in the thickness of the crucible wall. In addition, increasing thickness of the crucible wall increases the clearance between the inductor and crucible, resulting in a sharp drop in power factor.

Author Contributions: Conceptualization, H.Z. and D.T.; methodology, H.Z. and Y.Z.; software, Y.Z., S.C. and D.Z.; validation, H.Z., J.T. and D.Z.; formal analysis, H.Z. and D.T.; investigation, H.Z., Y.Z. and D.T.; resources, H.Z. and D.T.; data curation, Y.Z. and D.T.; writing—original draft preparation, H.Z., Y.Z. and D.T.; writing—review and editing, H.Z., Y.Z., D.T., S.C., J.T. and D.Z.; visualization, S.C., J.T. and D.Z.; supervision, H.Z. and D.T.; project administration, H.Z. and J.T.; funding acquisition, H.Z. All authors have read and agreed to the published version of the manuscript.

Funding: This research was funded by the Fund project [202111342010] supported by the China innovation training program for College Students.

Data Availability Statement: All data used to support the findings of this study are included within the article.

Conflicts of Interest: The authors declare no conflict of interest.

References

1. Zhang, Z.; Ye, J.; Tan, D.; Feng, Z.; Luo, J.; Tan, Y.; Huang, Y. The effects of Fe_2O_3 based DOC and SCR catalyst on the combustion and emission characteristics of a diesel engine fueled with biodiesel. *Fuel* **2021**, *290*, 120039. [CrossRef]
2. Zhang, Z.; Tian, J.; Xie, G.; Li, J.; Xu, W.; Jiang, F.; Huang, Y.; Tan, D. Investigation on the combustion and emission characteristics of diesel engine fueled with diesel/methanol/n-butanol blends. *Fuel* **2022**, *314*, 123088. [CrossRef]
3. Yuan, S.; Dai, Z.; Zhou, Z.; Chen, X.; Yu, G.; Wang, F. Rapid co-pyrolysis of rice straw and a bituminous coal in a high-frequency furnace and gasification of the residual char. *Bioresour. Technol.* **2012**, *109*, 188–197. [CrossRef]
4. Pereira, L.; Martinez, L.; Mucsi, C.; Reis, L.; Rossi, J. On the melting of zirconium alloys from scraps using electron beam and induction furnaces–recycling process viability. *J. Mater. Res. Technol.* **2020**, *9*, 4867–4875. [CrossRef]
5. Jiménez, E.; Béjar, L.; Aguilar, C.; López, I.; Hernandez, O. Microstructural characterization of the Ti-30Nb-6Sn alloy synthesized by mechanical alloying. *Microsc. Microanal.* **2021**, *27*, 574–576. [CrossRef]
6. Zhang, Z.; Ye, J.; Lv, J.; Xu, W.; Tan, D.; Jiang, F.; Huang, H. Investigation on the effects of non-uniform porosity catalyst on SCR characteristic based on the field synergy analysis. *J. Environ. Chem. Eng.* **2022**, *10*, 107056. [CrossRef]

7. Ramanathan, A.; Krishnan, P.; Muraliraja, R. A review on the production of metal matrix composites through stir casting—Furnace design, properties, challenges, and research opportunities. *J. Manuf. Processes* **2019**, *42*, 213–245. [CrossRef]
8. Stanchev, V. Consulting expert system for coreless induction furnaces control. *IFAC Proc. Vol.* **2006**, *39*, 171–176. [CrossRef]
9. Buliński, P.; Smolka, J.; Golak, S.; Przylucki, R.; Palacz, M.; Siwiec, G.; Lipart, J.; Bialecki, R.; Blacha, L. Numerical and experimental investigation of heat transfer process in electromagnetically driven flow within a vacuum induction furnace. *Appl. Therm. Eng.* **2017**, *124*, 1003–1013. [CrossRef]
10. Chen, Z.; Ma, W.; Li, S.; Wu, J.; Wei, K.; Yu, Z.; Ding, W. Influence of carbon material on the production process of different electric arc furnaces. *J. Clean. Prod.* **2018**, *174*, 17–25. [CrossRef]
11. Zhou, Q.; Wen, J.; Wu, J.; Ma, W.; Xu, M.; Wei, K.; Zhang, Z.; Zhang, L.; Xu, J. Recovery and purification of metallic silicon from waste silicon slag in electromagnetic induction furnace by slag refining method. *J. Clean. Prod.* **2019**, *229*, 1335–1341. [CrossRef]
12. Staroducbtsev, Y.; Tsepelev, V. Analysis of lossed in soft magnetic nanocrystalline alloys as a function of induction and frequency. *J. Magn. Magn. Mater.* **2020**, *500*, 166346.
13. Hsieh, C.; Hsu, H.; Mo, C.; Chen, Y.; Pai, C. Medium-frequency induction sintering of lithium nickel cobalt manganese oxide cathode materials for lithiumion batteries. *Solid State Ion.* **2015**, *270*, 39–46. [CrossRef]
14. Asad, A.; Kratzsch, C.; Dudczig, S.; Aneziris, C.; Schwarze, R. Numerical study of particle filtration in an induction crucible furnace. *Int. J. Heat Fluid Flow* **2016**, *62*, 299–312. [CrossRef]
15. Yuan, X.; Zhang, T.; Xiang, Y.; Dai, X. Parallel chaos optimization algorithm with migration and merging operation. *Appl. Soft Comput.* **2015**, *35*, 591–604. [CrossRef]
16. Dwivedi, S.; Vardhan, M.; Tripathi, S. An Effect of Chaos Grasshopper Optimization Algorithm for Protection of Network Infrastructure. *Comput. Netw.* **2020**, *176*, 107251. [CrossRef]
17. Hajiheidari, S.; Wakil, K.; Badri, M.; Navimipour, N. Intrusion detection systems in the internet of things: A comprehensive investigation. *Comput. Netw.* **2019**, *160*, 165–191. [CrossRef]
18. Zakeri, A.; Hokmabadi, A. Efficient feature selection method using real-valued grasshopper optimization algorithm. *Expert Syst. Appl.* **2019**, *119*, 61–72. [CrossRef]
19. Li, H.; Wang, Y.; Zuo, Z. Chaos-based image encryption algorithm with orbit perturbation and dynamic state variable selection mechanisms. *Opt. Lasers Eng.* **2019**, *115*, 197–207. [CrossRef]
20. Chen, J.; Lin, Q.; Ji, Z. Chaos-based multi-objective immune algorithm with a fine-grained selection mechanism. *Soft Comput.* **2011**, *15*, 1273–1288. [CrossRef]
21. Guo, Z.; Wang, S.; Zhuang, J. A novel immune evolutionary algorithm incorporating chaos optimization. *Pattern Recognit. Lett.* **2006**, *27*, 2–8.
22. Xu, Q.; Zhang, C.; Sun, J.; Zhang, l. Adaptive Learning Rate Elitism Estimation of Distribution Algorithm Combining Chaos Perturbation for Large Scale Optimization. *Open Cybern. Syst. J.* **2016**, *10*, 20–40. [CrossRef]
23. Ghosh, P.; Mali, K.; Das, S. Chaotic Firefly Algorithm-Based Fuzzy C-Means Algorithm for Segmentation of Brain Tissues in Magnetic Resonance Images. *J. Vis. Commun. Image Represent.* **2018**, *54*, 63–79. [CrossRef]
24. Hong, L.; Kamruzzaman, J. A new convergence rate estimation of general artificial immune algorithm. *J. Intell. Fuzzy Syst.* **2015**, *28*, 2793–2800. [CrossRef]
25. Xu, H.; Li, P.; Cong, Z.; Zhang, F.; Pan, Y.; Ren, X.; Wang, X.; Xing, Y. Test Case Prioritization Based on Artificial Immune Algorithm. *Teh. Vjesn.-Tech. Gaz.* **2021**, *28*, 1871–1876.
26. Miralvand, M.; Rasoolzadeh, S.; Majidi, M. Proposing a features preprocessing method based on artificial immune and minimum classification errors methods. *J. Appl. Res. Technol.* **2015**, *13*, 477–481. [CrossRef]
27. Pánek, D.; Orosz, T.; Kropík, P.; Karban, P.; Dolezel, I. Reduced-Order Model Based Temperature Control of Induction Brazing Process. In Proceedings of the 2019 Electric Power Quality and Supply Reliability Conference (PQ) & 2019 Symposium on Electrical Engineering and Mechatronics (SEEM), Kärdla, Estonia, 12–15 June 2019.
28. Wang, S.; Huang, G.; Baetz, B.; Ancell, B. Towards robust quantification and reduction of uncertainty in hydrologic predictions: Integration of particle Markov chain Monte Carlo and factorial polynomial chaos expansion. *J. Hydrol.* **2017**, *548*, 484–497. [CrossRef]
29. Mehak, K.; Sankalap, A. Chaotic grey wolf optimization algorithm for constrained optimization problems. *J. Comput. Des. Eng.* **2017**, *4*, 458–472.
30. Chen, X.; Hu, C. Adaptive medical image encryption algorithm based on multiple chaotic mapping. *Natl. Libr. Med.* **2017**, *24*, 1821–1827. [CrossRef]
31. Vishal, K.; Agrawal, S. On dynamics, existence of chaos, control and synchronization of novel complex chaotic system. *Chin. J. Phys.* **2017**, *55*, 519–532. [CrossRef]
32. Xu, X.; Rong, H.; Pereira, E.; Trovati, M. Predatory Search-based Chaos Turbo Particle Swarm Optimization (PS-CTPSO): A new particle swarm optimisation algorithm for Web service combination problems. *Future Gener. Comput. Syst.* **2018**, *89*, 375–386. [CrossRef]
33. Marelli, S.; Sudret, B. An active-learning algorithm that combines sparse polynomial chaos expansions and bootstrap for structural reliability analysis. *Struct. Saf.* **2017**, *75*, 67–74. [CrossRef]
34. Zhang, X.; Wang, X. Multiple-image encryption algorithm based on mixed image element and chaos. *Comput. Electr. Eng.* **2017**, *62*, 401–413. [CrossRef]

35. Meng, J.; Li, H. An efficient stochastic approach for flow in porous media via sparse polynomial chaos expansion constructed by feature selection. *Adv. Water Resour.* **2017**, *105*, 13–28. [CrossRef]
36. Zhang, Y.; Zhao, Y.; Fu, X.; Xu, J. A feature extraction method of the particle swarm optimization algorithm based on adaptive inertia weight and chaos optimization for Brillouin scattering spectra. *Opticsunications* **2016**, *376*, 56–66. [CrossRef]
37. Gaganpreet, K.; Sankalap, A. Chaotic whale optimization algorithm. *J. Comput. Des. Eng.* **2018**, *5*, 275–284.
38. Hao, P.; Wang, Y.; Liu, C.; Wang, B.; Wu, H. A novel non-probabilistic reliability-based design optimization algorithm using enhanced chaos control method. *Comput. Methods Appl. Mech. Eng.* **2017**, *318*, 572–593. [CrossRef]
39. Wang, X.; Pei, W.; Atluri, S. Bifurcation & chaos in nonlinear structural dynamics: Novel & highly efficient optimal-feedback accelerated Picard iteration algorithms. *Commun. Nonlinear Ence Numer. Simul.* **2018**, *65*, 54–69.
40. Rizk-Allah, R.; Hassanien, A.; Bhattacharyya, S. Chaotic Crow Search Algorithm for Fractional Optimization Problems. *Appl. Soft Comput.* **2018**, *71*, 1161–1175. [CrossRef]
41. Cao, Z. Evolutionary optimization of artificial neural network using an interactive phase-based optimization algorithm for chaotic time series prediction. *Soft Comput.* **2020**, *24*, 17093–17109. [CrossRef]
42. Li, K.; Xue, W.; Mao, H.; Chen, X.; Jiang, H.; Tan, G. Optimizing the 3D Distributed Climate inside Greenhouses Using Multi-Objective Optimization Algorithms and Computer Fluid Dynamics. *Energies* **2019**, *12*, 2873. [CrossRef]
43. Abdulla, A.; Mamun, B. A survey of intrusion detection systems based on ensemble and hybrid classifiers. *Comput. Secur.* **2017**, *65*, 135–152.
44. Arora, S.; Anand, P. Chaotic grasshopper optimization algorithm for globaloptimization. *Neural Comput. Appl.* **2019**, *31*, 4385–4405. [CrossRef]
45. Adam, S.; Alexandropoulos, S.; Pardalos, P.; Vrahatis, M. No Free Lunch Theorem: A Review. *Approx. Optim.* **2019**, 57–82.
46. Orosz, T.; Rassõlkin, A.; Kallaste, A.; Arsenio, P.; Pánek, D.; Kaska, J.; Karban, P. Robust Design Optimization and Emerging Technologies for Electrical Machines: Challenges and Open Problems. *Appl. Sci.* **2020**, *10*, 6653. [CrossRef]
47. Fan, L.; Cheng, F.; Zhang, T.; Liu, G.; Yuan, J.; Mao, P. Visible-light photoredox-promoted desilylative allylation of a-silylamines: An efficient route to synthesis of homoallylic amines. *Tetrahedron Lett.* **2021**, *81*, 153357. [CrossRef]
48. Esfahani, M.; Hosseinian, S.; Vahidi, B. A new optimal approach for improvement of active power filter using FPSO for enhancing power quality. *Int. J. Electr. Power Energy Syst.* **2015**, *69*, 188–199. [CrossRef]
49. Tkacheva, O.; Arkhipov, P.; Zaykov, Y. Solid phase formation during aluminium electrolysis. *Electrochem. Commun.* **2020**, *110*, 106624. [CrossRef]
50. Dou, J.; Jia, X.; Huang, Z.; Gu, X.; Xia, M.; Zheng, Y.; Ma, B. Theoretical and experimental study on jet formation and penetration of the liner loaded by electromagnetic force. *Int. J. Mech. Sci.* **2020**, *186*, 105883.
51. Zhang, Z.; Li, J.; Tian, J.; Zhong, Y.; Zou, Z.; Dong, R.; Gao, S.; Xu, W.; Tan, D. The effects of Mn-based catalysts on the selective catalytic reduction of NO_x with NH_3 at low temperature: A review. *Fuel Process. Technol.* **2022**, *230*, 107213. [CrossRef]
52. Zuo, H.; Tan, J.; Wei, K.; Huang, Z.; Zhong, D.; Xie, F. Effects of different poses and wind speeds on wind-induced vibration characteristics of a dish solar concentrator system. *Renew. Energy* **2021**, *168*, 1308–1326. [CrossRef]
53. Zuo, H.; Liu, G.; Jiaqiang, E.; Zuo, W.; Wei, K.; Hu, W.; Tan, J.; Zhong, D. Catastrophic analysis on the stability of a large dish solar thermal power generation system with wind-induced vibration. *Sol. Energy* **2019**, *183*, 40–49. [CrossRef]
54. Hu, L.; Hu, X.; Che, Y.; Feng, F.; Lin, X.; Zhang, Z. Reliable state of charge estimation of battery packs using fuzzy adaptive federated filtering. *Appl. Energy* **2020**, *262*, 114569. [CrossRef]
55. Ma, Y.; Liu, C.; Jiaqiang, E.; Mao, X.; Yu, Z. Research on modeling and parameter sensitivity of flow and heat transfer process in typical rectangular microchannels: From a data-driven perspective. *Int. J. Therm. Sci.* **2022**, *172*, 107356. [CrossRef]
56. Gu, M.; Chu, H.; Liu, F. Effects of simultaneous hydrogen enrichment and carbon dioxide dilution of fuel on soot formation in an axisymmetric coflow laminar ethylene/air diffusion flame. *Combust. Flame* **2016**, *166*, 216–228. [CrossRef]
57. Chu, H.; Han, W.; Cao, W.; Gu, M.; Xu, G. Effect of methane addition to ethylene on the morphology and size distribution of soot in a laminar co-flow diffusion flame. *Energy* **2019**, *166*, 392–400. [CrossRef]
58. Ren, F.; Chu, H.; Xiang, L.; Han, W.; Gu, M. Effect of hydrogen addition on the laminar premixed combustion characteristics the main components of natural gas. *J. Energy Inst.* **2019**, *92*, 1178–1190. [CrossRef]
59. Chu, H.; Ya, Y.; Nie, X.; Qiao, F.; Jiaqiang, E. Effects of adding cyclohexane, n-hexane, ethanol, and 2, 5-dimethylfuran to fuel on soot formation in laminar coflow n-heptane/iso-octane diffusion flame. *Combust. Flame* **2021**, *225*, 120–135. [CrossRef]
60. Cai, T.; Zhao, D.; Wang, B.; Li, J.; Guan, Y. NO_x emission and thermal performances studies on premixed ammonia-oxygen combustion in a CO_2-free micro-planar combustor. *Fuel* **2020**, *280*, 118554. [CrossRef]
61. Cai, T.; Sun, Y.; Zhao, D. Enhancing heat transfer performance analyses of a hydrogen-fueled meso-combustor with staggered bluff-bodies. *Fuel Process. Technol.* **2021**, *218*, 106867. [CrossRef]
62. Chen, L.; Deng, Y.; Feng, C.; Han, W.; Jiaqiang, E.; Wang, C.; Han, D.; Zhang, B. Effects of zeolite molecular sieve on the hydrocarbon adsorbent performance of gasoline engine of during cold start. *Fuel* **2022**, *310*, 122427. [CrossRef]
63. Feng, C.; Deng, Y.; Tan, Y.; Han, W.; Jiaqiang, E.; Chen, L.; Han, D. Experimental and simulation study on the effect of ZSM-5 hydrocarbon catcher on the emission of gasoline engine during cold start. *Fuel* **2022**, *313*, 122661. [CrossRef]
64. Li, Y.; Tang, W.; Chen, Y.; Liu, J.; Lee, C. Potential of acetone-butanol-ethanol (ABE) as a biofuel. *Fuel* **2019**, *242*, 673–686. [CrossRef]
65. Li, Y.; Meng, L.; Nithyanandan, K.; Lee, T.; Lin, Y.; Lee, C.; Liao, S. Combustion, performance and emissions characteristics of a spark-ignition engine fueled with isopropanol-n-butanol-ethanol and gasoline blends. *Fuel* **2016**, *184*, 864–872. [CrossRef]

66. Tan, D.; Chen, Z.; Li, J.; Luo, J.; Yang, D.; Cui, S.; Zhang, Z. Effects of Swirl and Boiling Heat Transfer on the Performance Enhancement and Emission Reduction for a Medium Diesel Engine Fueled with Biodiesel. *Processes* **2021**, *9*, 568. [CrossRef]
67. Zhang, Z.; Jiaqiang, E.; Chen, J.; Zhao, X.; Zhang, B.; Deng, Y.; Peng, Q.; Yin, Z. Effects of Boiling Heat Transfer on the Performance Enhancement of a Medium Speed Diesel Engine Fueled with Diesel and Rapeseed Methyl Ester. *Appl. Therm. Eng.* **2020**, *169*, 114984. [CrossRef]
68. Huang, Z.; Huang, J.; Luo, J.; Hu, D.; Yin, Z. Performance enhancement and emission reduction of a diesel engine fueled with different biodiesel-diesel blending fuel based on the multi-parameter optimization theory. *Fuel* **2022**, *314*, 122753. [CrossRef]